ACS APPLIED MATERIALS & INTERFACES

Open Access

This article is licensed under CC-BY 4.0

www.acsami.org

Research Article

Effects of Polyaromatic Film Interfaces on Cu Catalysts for Selective Electrochemical CO_2 Reduction

Gerard Martí, Andreina Alarcón, Matilda Kraft, Arnau Carné-Sánchez, Marcos Gil-Sepulcre, Olaf Rüdiger, Serena DeBeer, Jordi García-Antón, Teresa Andreu, Antoni Llobet,* and Xavier Sala*

Cite This: *ACS Appl. Mater. Interfaces* 2026, 18, 50681−50693

Read Online

ACCESS | Metrics & More | Article Recommendations | Supporting Information

ABSTRACT: Electrochemical CO_2 reduction (CO_2RR) offers a sustainable pathway to convert CO_2 into energy-dense fuels and value-added chemicals, addressing both climate and energy storage challenges. This study investigates the effect of polyaromatic film (PAF) coatings on Cu-based catalysts with distinct morphologies (cubes, porous spheres, and small nanoparticles) and compositions (ranging from metallic Cu, to Cu_2O and CuO). PAF functionalization modulates the competition between CO_2RR and HER in a catalyst- and potential-dependent manner, leading to selective enhancement of C_{2+} products for specific Cu catalyst types and applied potentials. Notably, PAF-coated Cu_2O porous spheres (**Cu_2O-PSph/PAF**) achieved a maximum multicarbon faradaic efficiency of 63% at −1.40 V vs RHE while sustaining a total current density of 16 mA·cm^{-2}. Under high-current density (−127 mA·cm^{-2}) flow-cell conditions, **Cu_2O-PSph/PAF** maintained stable activity for over 80 min, whereas the uncoated analogue exhibited a fast decrease of C_{2+} production, highlighting the stabilizing role of the polymeric layer during operation. In addition, the PAF coating influences catalyst evolution by partially confining soluble Cu^+ species, reducing particle fragmentation, and guiding aggregate formation. Overall, these findings demonstrate that PAF functionalization not only enhances CO_2RR selectivity but also improves operational stability and directs the morphological evolution of Cu catalysts under catalytic turnover, offering a versatile strategy for high-performance CO_2 electroreduction.

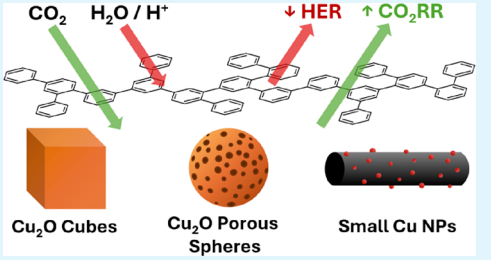

KEYWORDS: *CO_2 electroreduction, polyaromatic films, electrocatalysis, nanocatalysis, multicarbon products, copper*

1. INTRODUCTION

Anthropogenic CO_2 emissions remain a major contributor to global warming and climate change.[1−3] Accordingly, considerable efforts are being directed to develop strategies for its capture and conversion, aiming at a more sustainable society.[4−6] In this regard, the electrochemical CO_2 reduction reaction (CO_2RR) for the production of fuels and value-added products has emerged as a promising alternative to enable industrial sustainability and, ideally, to reach a circular carbon economy.[7,8] A wide variety of metal-based species have been studied in recent years as electrocatalysts for the CO_2RR.[9,10] However, the suppression of the more favorable HER in aqueous media and the selectivity toward multicarbon (C_{2+}) high energy-density products (i.e., hydrocarbons and oxygenates) remain a major challenge in the field.[11−15]

The ability of Cu to couple CO_2R reaction intermediates and form C–C bonds are key features when targeting C_{2+} compounds.[16−18] In the recent years, many studies have shown how different parameters of Cu particles affect their product selectivity.[19,20] For example, Buonsanti and coworkers demonstrated that octahedral Cu particles, with exposed (111) facets, are more selective toward CH_4, while the (100) facets of cubic particles are more selective for C_2H_4 and spheric particles do not show any specific selectivity.[21] On the other hand, the starting oxidation state of the particles has also been shown to be relevant for catalyst selectivity.[22,23] The presence of oxides generates undercoordinated Cu atoms, causes surface strain, and grants the presence of oxidic Cu species under catalytic conditions, favoring the selective reduction of CO_2 to C_{2+}. More recently, heterometallic Cu-based catalysts have also emerged as an effective strategy to promote C_{2+} formation, where synergistic interactions between Cu and secondary metal sites (e.g., Zn) modulate the adsorption of key intermediates, increase local CO coverage, and facilitate C–C coupling.[24−26] Finally, spatial confinement effects, which influence mass transport (e.g., CO_2 availability), local pH, and the distribution of key reaction intermediates (such as *CO, *CO–CO, and *CO–CHO), have also been shown to play a crucial role.[19] Accordingly, numerous studies highlight the importance of catalyst porosity in promoting the efficient formation of C_2 and C_3

Received: March 23, 2026
Revised: July 20, 2026
Accepted: August 11, 2026
Published: September 10, 2026

Downloaded from pubs.acs.org/aamick/article-pdf/18/37/50681/6847838/am-2026-05380r.pdf by guest on 21 October 2026

© 2026 The Author(s). Published by American Chemical Society

products during CO_2 electroreduction on Cu-based materials.[27−29]

Beyond controlling the morphology, composition, and oxidation state of Cu catalysts, a wide range of surface-modification strategies have recently emerged to promote C_{2+} formation during CO_2RR. As reviewed by Tan et al., these approaches include the incorporation of metallic and nonmetallic species, molecular modifiers, polymeric coatings, and carbon-based overlayers.[33] Despite their diversity, these strategies generally operate through a limited set of mechanistic principles, namely, tuning the electronic structure and oxidation state of Cu, stabilizing key reaction intermediates, increasing local *CO coverage, regulating proton availability, and engineering the catalyst–electrolyte microenvironment. These effects can facilitate C–C coupling by lowering the energy barrier for *CO dimerization or *CO–*CHO coupling and by creating confined interfacial environments that increase the local concentration and residence time of reactive intermediates. Among these approaches, polymeric coatings have attracted particular interest because they can simultaneously regulate mass transport and the local interfacial environment while maintaining the intrinsic catalytic properties of the underlying Cu catalyst.[9,30−33] However, in most cases, polymer and catalyst are mixed to make an ink, which is later deposited on an electrode.[34−36] This strategy makes it difficult to assess the real distribution and interactions between the polymer and the catalyst, preventing an accurate rationalization of its effect on the CO_2RR. Recent reports have studied the direct electropolymerization of organic films on Cu electrodes.[37−39] Lima and Venkatkarthick used pyrrole and thiophene electropolmerization on Cu electrodes, which resulted in enhanced ethylene generation.[38] Peters et al. studied the effect of polyaromatic films (PAF) on Cu electrodes, which resulted in an enhancement in the C_{2+} faradaic efficiency (FE) from 26% for bare Cu to 70% for the PAF-coated Cu.[39] However, despite the growing interest in surface-modification strategies for Cu-based CO_2RR catalysts, studies have primarily focused on planar Cu electrodes or catalyst/polymer mixtures, and the influence of directly electropolymerized coatings on shape- and composition-controlled Cu particles remains largely unexplored. In particular, the interplay between particle morphology, catalyst restructuring, and interfacial polymer layers during CO_2RR has not been systematically investigated.

The evolution of Cu catalysts under cathodic potentials is a relevant parameter in electrocatalytic CO_2RR. It is well known that Cu-based materials, even in the case of Cu electrodes, suffer from fragmentation, dissolution/redeposition, and coalescence processes.[40−45] These morphological changes can also induce variations in the performance of the catalysts, having an impact on product selectivity.[45−47] Despite the advancements in the field, the effect of polymeric coatings on the evolution of Cu-based particles under CO_2RR turnover has not yet been assessed.

In the present work, we study the effect of electropolymerized PAFs on Cu-based particles with distinct morphologies: cubes, porous spheres, and small Cu nanoparticles (NPs). These materials were synthesized by means of salt reduction and organometallic approaches, followed by diphenyliodonium triflate (DPITfO) electropolymerization to form PAF coatings. Comprehensive characterization of materials before and after catalysis together with detailed quantification of CO_2RR products enables us to rationalize the morphology-dependent effect as well as the influence of the PAF coatings. The hydrophobic PAF layers influence not only product selectivity but also the structural evolution of the catalysts under cathodic potential. Moreover, the functionalization strategy has been extended to a flow cell configuration to assess its scalability toward enhanced C_{2+} product generation.

2. EXPERIMENTAL METHODS

2.1. Chemicals and Reagents

All procedures involving the synthesis of Cu-based materials by salt reduction methods were carried out using standard glassware, round-bottom flasks, and Dimroth condensers. Procedures involving the organometallic synthetic approach were carried out using tightly sealed Fischer-Porter vessels and under inert conditions, either in a glovebox (MBRAUN UNIlab workstation 9950) or in a Schlenk line. All glassware was washed with acid and properly rinsed and dried at 100 °C for several hours before each use. Reactions were heated in oil baths with controlled temperature. Copper(II) acetate monohydrate was purchased from J·T.Baker Chemicals. Dimethyl sulfoxide (DMSO), potassium hexacyanoferrate(II) ($K_4[Fe(CN)_6]$), potassium chloride, ethylene glycol, absolute ethanol, sodium hydroxide, potassium hydroxide, D-(+)-glucose, 1-propanol (1-PrOH), copper chloride dihydride, L-ascorbic acid, and diphenyliodonium triflate (DPITfO) were purchased from Merck. Mesityl copper(I) was purchased from STREM Chemicals. Ethanol 96% for the washing steps of materials was purchased from Labkem. The water used in the experiments was in all cases Milli-Q water with resistivity between 17 and 19 MΩ·cm. Toluene for organometallic synthesis was dried over sodium and degassed by means of the freeze–pump–thaw methodology to ensure the absence of oxygen. THF for suspensions was dried over sodium/benzophenone. Carbon paper (CP, Sigracet 39 AA) and carbon cloth (CT Carbon Cloth with MPL-W1S1011) were purchased from FuelCell store, and the gas diffusion layer (GDL, Freudenberg H23C6) was acquired from Quintech. All CP pieces were washed by sonicating them in isopropanol for 15 min and then in hexane for 15 more minutes and properly dried before its use. Carbon cloth was submerged in acetone and dried before its use. Gas mixtures containing H_2, CO_2, CO, CH_4 and C_2H_4, C_2H_6 for gas chromatography calibration were purchased from Linde. Deuterium oxide for NMR was purchased from Eurisotop.

2.2. Synthetic Procedures

2.2.1. Synthesis of Cu_2O Cubes (Cu_2O-Cub). **Cu_2O-Cub** cubes were synthesized following previously described methods.[48] The final material was stored at ambient conditions.

2.2.2. Synthesis of Cu_2O Porous Spheres (Cu_2O-PSph). **Cu_2O-PSph** porous spheres were synthesized by adapting a previously described method.[49] First, 0.50 g of $Cu(OAc)_2{\cdot}H_2O$ was dissolved in a mixture of water and organic solvents (5.0 mL of water, 10.0 mL of ethylene glycol, and 25.0 mL of absolute ethanol). The solution was heated up to 70 °C in an oil bath, and 0.70 g of NaOH was added to it. The solution was left to stir for 30 min before adding 0.54 g of D-(+)-glucose. At this point, the reaction was let to evolve for 4 min and then rapidly cooled down by immersing the flask in an ice bath, where it is left to cool down for 10 min. The material was filtered and washed three times with water and three times with ethanol before drying it under vacuum for at least 4 h. The final material was left 1 month at ambient conditions and then preserved under inert atmosphere.

2.2.3. Synthesis of Cu Nanoparticles Supported on Carbon Paper (Cu-Org). **Cu-Org** were synthesized by adapting previously described methods for Cu NPs in suspension.[50] The synthetic process was conducted under inert-atmosphere conditions, either using a Schlenk line or a glovebox. First, 5.5 mg of mesityl copper(I) was added to a Fischer-Porter vessel and dissolved in 20.0 mL of dry and

Downloaded from pubs.acs.org/aamick/article-pdf/18/37/50681/6847837/am-2026-05380r.pdf by guest on 21 October 2026

https://doi.org/10.1021/acsami.6c05380
ACS Appl. Mater. Interfaces 2026, 18, 50681−50693

degassed toluene. A piece of carbon paper (CP, 0.5 cm × 3.5 cm, 10.2 mg) was introduced (and completely submerged) into the solution. The Fischer-Porter vessel was then tightly closed, pressurized with 3 bars of H_2, and placed in an oil bath at 110 °C. The reaction was let to evolve for 10 h and left to cool down at room temperature before removing the hydrogen. The resulting material was washed three times with toluene and dried under vacuum for at least 45 min. The final material was stored in the glovebox.

2.3. Electrode Preparation and Electrochemical Testing

Electrode Preparation for Gas-Tight H-Cell Experiments. In the case of **Cu_2O-PSph** and **Cu_2O-Cub**, 2.0 mg of particles was suspended in 2.0 mL of THF. From this suspension, four drops of 10.0 μL were drop cast on each side of CP pieces (1.0 cm × 0.5 cm), letting them dry between each drop addition. In the case of the organometallic Cu NPs (**Cu-Org**), the modified CP obtained already contained the Cu NPs. The pieces were cut in half to obtain two electrodes from each synthesis. ICP determined that the Cu loading on **Cu-Org** electrodes was 0.20% w/w. Finally, a piece of conductive copper tape was attached to each piece of the CP-based electrodes and Teflon tape was used to adjust the exposed area of electrodes to be used in CO_2 electroreduction.

Electrode Preparation for Flow Cell Experiments. For the flow cell system, 4.0 mg of **Cu_2O-PSph** suspended on 2.0 mL of THF was drop-cast on a 4 cm^2 GDL.

Generation of PAF Coatings. PAFs were generated in a one-compartment cell containing an aqueous CO_2-saturated (0.10 M $KHCO_3$) 10 mM diphenyliodonium triflate (DPITfO) solution. To generate the PAFs, –0.90 V vs RHE was applied for 10 min. After that, the electrode was removed from a gas-tight H-cell, rinsed with Milli-Q water, and left to dry before its use.

Electrochemical CO_2RR on the Gas-Tight H-Cell. The setup for electrochemical CO_2 reduction consisted of the gas-tight H-cell with two compartments separated by a glass membrane (3 Å pore size). The working (WE) and reference electrodes (RE), carbon paper with the CuO_x material and Ag/AgCl (3.0 M NaCl), respectively, were placed in one compartment and the counter electrode (CE), a platinum wire, in the other one. The WE was fixed by a crocodile clip connected to the copper tape stuck to the carbon paper. All metallic parts were covered with Teflon to avoid the electrolyte contacting any metallic component. Once the cell was tightly closed with septa, the compartments were purged with CO_2 by bubbling the gas for 15 min, obtaining a CO_2-saturated electrolyte (pH = 6.8). CO_2 electroreduction was performed using an OrigaFlex 01A potentiostat by applying a fixed reductive potential for 1 h if not otherwise stated. Each experiment was done using a new electrode and results are given as the average value of two independent measurements together with the corresponding error bars. Linear sweep voltammetries (LSV) were performed at 100 mV/s scan rate ranging from –210 to –2200 mV vs Ag/AgCl or CE overload. Chronoamperometries (CA) were performed by applying the chosen potential for 1 h. The overall charge that went through the system could be obtained by integrating the current density (j) vs time (t) curve. All reference potentials were converted to reversible hydrogen electrode (RHE) as follows: $E_{RHE} = E_{Ag/AgCl} + E_{Ag/AgCl}^{0} + 0.059 \cdot pH$, where $E_{Ag/AgCl}^{0} = 0.197$ V and $E_{Ag/AgCl}$ is the applied working potential.

Electrochemical CO_2RR on a Flow Cell. The setup consisted of an H-type electrochemical cell (FlexCell-PP, Gaskatel) with two compartments separated by a proton exchange membrane (PEM, Nafion 115). The cathodic and anodic compartments were filled with 15.0 mL of CO_2-saturated 0.50 M $KHCO_3$ and 25.0 mL of 1.50 M KOH aqueous solutions, respectively. The CO_2 flow rate on the back side of the cathode was fixed at 150 mL·min^{-1} by using a mass flow controller (Bronkhorst). The WE and RE, the GDE containing the Cu catalyst and a hydrogen reference electrode (Hydroflex(M-v01-0071)), respectively, were placed on the cathodic compartment, while the CE (a Pt mesh) was placed in the anodic compartment. CO_2 electroreduction was performed by applying a fixed current density (j), ranging from –32 to –127 mA·cm^{-2}, for 20 min using a BioLogic (SP-150e) potentiostat. One same electrode was used consecutively from lower to higher j to obtain the product selectivity of the system, just rinsing the cathodic compartment with 0.50 M aqueous $KHCO_3$ and replacing the electrolyte on the cathodic side before the following measurement. The given results correspond to single measurements.

Product Analysis in Gas-Tight H-Cell Experiments. Gaseous products were analyzed by means of an Agilent 8890 gas chromatograph (GC) containing three different chromatography columns connected in parallel (DB-1, HP-MOLESIEVE, and HP-PLOT/Q) for proper peak separation and resolution. A thermal conductivity detector (TCD) was used to measure hydrogen, while a methanizer combined with a flame ionization detector (FID) was used to measure carbon-based products with higher sensitivity. When an electrochemical experiment was finished, 0.5 mL of the cathodic headspace (where the CO_2 reduction takes place) were injected in the GC using a tight lock Hamilton syringe. To quantify the products, the GC was calibrated by using three different reference mixtures of H_2, CO, CH_4, and C_2H_4, and the volume of the cathodic headspace was measured beforehand. Formate ($HCOO^-$) and ethanol (EtOH) were quantified by means of nuclear magnetic resonance (NMR) spectroscopy using a Bruker 300 MHz Ascend instrument with an AVANCE NEO nanoconsole, AVAILABLE PROBE, and BCU-05 complement for sample temperature control. Samples for analysis were prepared by mixing 650 μL of electrolyte with 50 μL of a 10 mM DMSO solution in D_2O. DMSO was used as an internal pattern for the proper quantification of the products. All measurements were performed with water signal suppression to maximize the signals of DMSO and the products of interest. 1-Propanol (1-PrOH) was quantified by means of an Agilent 8890 gas chromatograph equipped with an HP-FFAP column and an FID detector. For the measurements, 2.0 μL of liquid sample was injected applying a 2:1 split ratio, and a 13.2 μM 1-PrOH solution in 0.10 M $KHCO_3$ was used as an external pattern. Exemplary chromatograms for the detection of the reaction products can be found in Figures S29–S35.

Product Analysis in Flow Cell Experiments. In this case, gaseous products were measured by an on-line gas chromatography system (990 Micro GC, Agilent) whose inlet was directly connected to the flow cell. H_2, CO, and CH_4 were detected through one channel containing a MS5A SS column and a TCD detector, while CO_2 and multicarbon products (C_2H_4 and C_2H_6) were detected through a second channel containing a PoraPLOT U column and a TCD detector. Calibration of the GC was done using gas mixtures of known concentrations. Liquid products were quantified by means of proton nuclear magnetic resonance (^{1}H-NMR) spectroscopy using a Bruker 400 instrument. Samples for analysis were prepared by mixing 490 μL of electrolyte with 90 μL of deuterium oxide (D_2O) and 20 μL of 0.2% v/v DMSO aqueous solution as internal standard. All measurements were performed with water signal suppression to maximize the signals of DMSO and the products of interest.

2.4. Characterization Techniques

High-Resolution Transmission Electron Microscopy (HRTEM). TEM analysis was performed at the Servei de Microscòpia de la UAB by means of a JEM-2011 unit with a 200 kV acceleration voltage. Samples were prepared by drop-casting the crude suspension of the materials on carbon-coated copper grids. Pictures were treated by means of Fiji ImageJ, an image processing freeware. In each sample, at least 100 NPs from four different regions of a grid were measured to ensure representative results for all Cu-based materials.

High-Resolution Scanning Electron Microscopy (HRSEM). Scanning electron microscopy analyses were performed either at Servei de Microscòpia de la UAB, at Centres Científics i Tecnològics (CCiTUB), or at Institut Català de Nanociència i Nanotecnologia (ICN2). The UAB microscope was a Zeiss Merlin module, which also allows analytical and compositional analysis using

Downloaded from pubs.acs.org/aamick/article-pdf/18/37/50681/6847838/am-2026-05380r.pdf by guest on 21 October 2026

https://doi.org/10.1021/acsami.6c05380
ACS Appl. Mater. Interfaces 2026, 18, 50681–50693

energy-dispersive X-ray spectroscopy (EDX). The ICN2 microscope was a Magellan 400 L module with a monochromator, UC (UniColore) Technology. All samples were prepared depositing part of the sample, dust, or piece of electrode, on a stub having conductive carbon tape at the surface. The obtained pictures were treated by means of Fiji ImageJ. In each sample, at least 100 NPs from four different regions of a grid were measured to ensure representative results for all Cu-based hybrid materials. In the case of morphological analysis, images from at least four different regions were taken to ensure their representativeness.

Isothermal Nitrogen Adsorption–Desorption. Isothermal nitrogen adsorption analysis at 77 K was performed at Catalan Institute of Nanoscience and Nanotechnology (ICN2) using an ASAP 2460 surface area and porosimetry system. Materials were submitted to thermal treatment at 120 °C under dynamic vacuum before measurements. Pore width distribution (PWD) and cumulative pore volume (CPV) were calculated by means of MicroActive 4.06 de Micromeritics software, using a DFT model considering cylindrical mesopores (HS-2D-NLDFT, Cab Cyl Mesopores, N2@77 K) and using a regularization factor of 0.1.

X-ray Diffraction (XRD). X-ray diffraction analyses were performed at Servei de Difracció de Raigs-X de la UAB by means of an X'Pert Powder powder diffractometer from Panalytical, with theta–theta geometry, copper anode (Kα Cu radiation λ = 1.5418 Å), and PIXcel^{1D} detector.

Inductively Coupled Plasma–Optical Emission Spectroscopy (ICP-OES). ICP-OES analyses were performed at Servei d'Anàlisi Química de la UAB by means of an acidic digestion and using an Agilent Optima model.

X-ray Photoelectron Spectroscopy (XPS). XPS was performed at Institut Català de Nanociència i Nanotecnologia (ICN2) by means of a SPECS instrument equipped with a Phoibos 1509-MCD detector using Kα Mg ($h\nu$ = 1235.6 eV) and Kα Al ($h\nu$ = 1483.6 eV) radiation from a dual source and keeping the pressure around 12–13 mbar during the measurements. The treatment of the spectra was done using CASAXPS software, setting the C 1s signal of adventitious carbon as reference at 285.0 eV.

Electrochemically Active Surface Area (ECSA). The ECSA is calculated upon the double-layer capacitance of the system (C_{DL}). This value can be estimated experimentally by means of cyclic voltammetry (CV). If one assumes that the measured current in non-faradaic regions arises from double-layer charging, the current can be expressed as the product of C_{DL} and the scan rate, as shown in eq 1. For this work, the non-faradaic region chosen is a potential window of 100 mV around the OCP (300 mV vs Ag/AgCl in 0.1 M $KHCO_3$).

$$I = \nu C_{DL} \quad (1)$$

Thus, plotting I as a function of ν will yield a straight line where the slope is C_{DL}. Hence, eight CVs at different scan rates (5, 10, 25, 50, 75, 100, 250, and 500 mV s^{-1}) were performed and the current at 300 mV *vs* Ag/AgCl was plotted. The ECSA was then obtained by dividing the calculated C_{DL} by the specific capacitance (C_S) of glassy carbon (eq 2).

$$\mathrm{ECSA} = \frac{C_{DL}}{C_S} \quad (2)$$

Contact Angle Measurements (CAM). CAMs were carried out using a contact angle device OCA35 from DataPhysics at standard climate conditions. Prior to measurements, 10 μL droplets of Milli-Q water were pipetted on the catalyst layer side of the gas diffusion electrodes. Sequentially, the drop shape analysis was done by Young–Laplace fitting. For each sample, at least three droplets were measured, and an average value was determined, whereby the error represents the standard deviation (±1).

XAS Measurements. Powder samples were prepared by diluting the corresponding Cu-based material with cellulose in a pellet (φ = 6 mm), followed by placement in the sample holder and sealing with 30 μm Kapton tape. The electrodes were prepared by drop-casting a 1 mg/mL suspension of the corresponding powder samples in THF on a carbon cloth electrode. In the case of **Cu-Org**, the NPs were synthesized on the carbon cloth support, following the previously described method on carbon paper. The generation of the electropolymerized PAF films was done following the same method explained for the carbon paper-based electrodes.

The Cu K-edge was utilized to conduct measurements on **Cu_2O-Cub**, **Cu_2O-PSph**, Cu(0), Cu_2O, and CuO in transmission mode. Prepared electrodes **Cu-Org**, **Cu_2O-Cub/PAF**, **Cu_2O-PSph/PAF**, and **Cu-Org/PAF** and cathodes for operando experiments were analyzed in fluorescent mode using a Multichannel Silicon-drift fluorescence detector. For the *operando* experiments, a custom-built spectroelectrochemical (SEC) flow cell was used.[51] The cell uses carbon cloth electrodes (CC, Fuelcell) functionalized with our systems. The aqueous electrolyte was bubbled with CO_2 before the measurements and pumped through the cell using a peristaltic pump. Spectra were acquired at beamline CLAESS (Static Cu K-edge XAS and EXAFS) at ALBA synchrotron with the collaboration of beamline scientists and ALBA staff. The incident energy was selected by a Si (311) double-crystal monochromator. Incident flux was *ca.* 5 × 10^{11} ph/s using a beam size of 250 μm × 500 μm. Incident energy was calibrated by assigning the first inflection point of Cu foil to 8979 eV. Final spectra were processed and normalized using the Athena program, included in the DEMETER package.[52]

Electrochemical Impedance Spectroscopy (EIS). Measurements were performed in a one-compartment cell, using Pt wire as the counter electrode, Ag/AgCl (sat. KCl) as the reference electrode, and a carbon paper with the catalyst as the working electrode, as prepared for electrochemical CO_2RR. Experiments were carried out in 0.10 M KCl solution containing 10 mM concentration of $K_4[FeCN)_6]$. Experiments were recorded by a PalmSense4 potentiostat at 0.24 V vs Ag/AgCl (sat. KCl), where the half peak potential of the redox $[FeCN)_6]^{3-}/[FeCN)_6]^{4-}$ couple is found. The amplitude was set to 10 mV, and the frequency ranged from 10^5 to 10^{-1} Hz, while the equilibration time was 5 s.

3. RESULTS AND DISCUSSION

3.1. Characterization of the Cu-Based Materials

Three different materials have been synthesized following different synthetic routes, as shown in Figure 1a. In each process the reaction conditions were chosen to obtain particles of radically different morphology. Cubes were formed starting from $CuCl_2$ and ascorbic acid as reducing agent,[48] porous spheres were obtained from $Cu(OAc)_2{\cdot}H_2O$ and glucose as reducing agent,[49] and supported Cu NPs were obtained by reducing [Cu(mes)] (mes = 1,3,5-trimethylbenzene) with molecular hydrogen.[50]

Scanning electron microscopy of the resulting materials (Figure 1b–d) shows the obtaining of cubes of 225 ± 85 nm (Figure S1a), porous spheres of 0.73 ± 0.17 μm (Figure S1b), and small NPs supported on carbon paper (CP) of 8.2 ± 3.7 nm (Figure S1c). For **Cu_2O-PSph**, TEM analysis of the reaction crude before centrifugation and washing showed the presence of small 2.42 ± 0.55 nm particles (Figure S2). These small particles self-assemble and form the final porous spheres observed by SEM (Figure 1c).[49] The three synthetic routes resulted not only in distinct morphologies but also in the generation of different Cu species in each specific case. Analysis by electron diffraction of **Cu_2O-Cub** (Figure 2a) showed the presence of the expected Cu_2O crystalline phase,[53] while its XPS spectra (Figure 2d) determined the presence of Cu_2O (peaks at 932.5 and 952.4 eV)[54] and a CuO passivating layer at the

Downloaded from pubs.acs.org/aamick/article-pdf/18/37/50681/6847838/am-2026-05380r.pdf by guest on 21 October 2026

https://doi.org/10.1021/acsami.6c05380
ACS Appl. Mater. Interfaces 2026, 18, 50681−50693

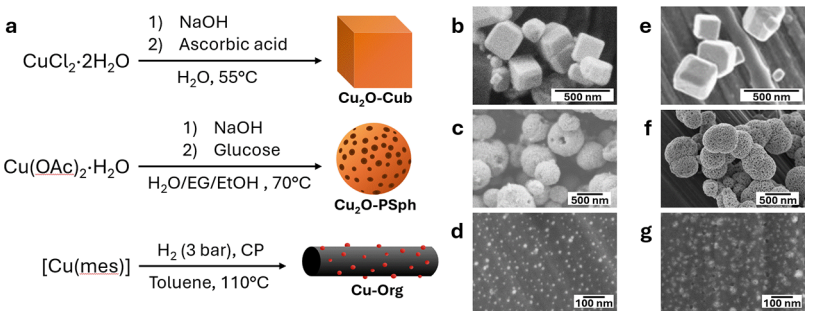

Figure 1. Simplified representation of the synthetic routes to obtain the different Cu-based materials (a) and HRSEM images of **Cu_2O-Cub** (b), **Cu_2O-PSph** (c), **Cu-Org** (d), **Cu_2O-Cub/PAF** (e), **Cu_2O-PSph/PAF** (f), and **Cu-Org/PAF** (g). EG = ethylene glycol.

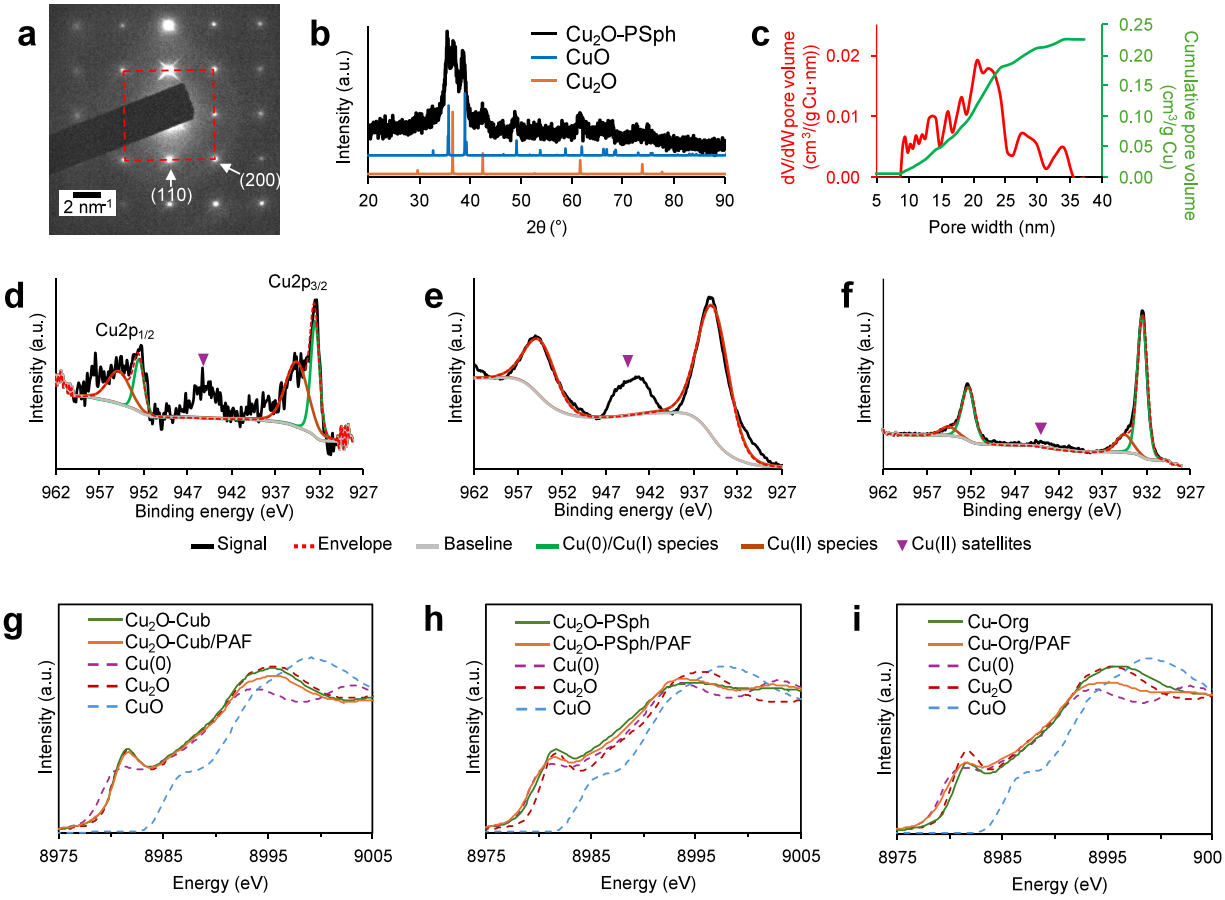

Figure 2. Electron diffraction pattern of **Cu_2O-Cub** (a). XRD spectra (b) and pore size distribution of **Cu_2O-PSph** (c). Cu $2p_{3/2}$ and $2p_{1/2}$ XPS spectra of **Cu_2O-Cub** (d), **Cu_2O-PSph** (e), and **Cu-Org** (f). Normalized Cu K-edge XANES spectra of **Cu_2O-Cub** (g), **Cu_2O-PSph** (h), and **Cu-Org** (i) and their PAF-functionalized analogues, along with Cu(0), CuO, and Cu_2O references. Reference XRD spectra were simulated with structures available in the crystallography open database.[56]

cubes surface (peaks at 934.8 and 954.5 eV together with satellite peaks).[55] XRD of **Cu_2O-PSph** (Figure 2b) indicated the presence of two mixed phases, CuO and Cu_2O,[56] while its surface-sensitive XPS spectra (Figure 2e) showed CuO as the only species at the particles surface.[55] The latter can be attributed to the complete oxidation of the outer Cu_2O layer during the applied passivation (4 weeks) at ambient conditions. This way, a Cu_2O/CuO mixed composition is obtained. Additional N_2 adsorption measurements of **Cu_2O-PSph** confirmed the mesoporous nature of the material (Figure 2c and Figure S3), showing a type IV(a) isotherm[57] and having pores in the size range of 9–35 nm. For **Cu-Org**, XPS analysis revealed the predominance of Cu(0)/Cu(I) species, which are difficult to distinguish by this technique,[54] along with a minor contribution from Cu(II) species (Figure 2f). Based on the synthetic route employed for Cu-Org, the formation of metallic Cu(0) particles is expected, consistent with the intense XPS signal assigned to Cu(0)/Cu(I). However, brief exposure of the

https://doi.org/10.1021/acsami.6c05380
ACS Appl. Mater. Interfaces 2026, 18, 50681−50693

Downloaded from pubs.acs.org/aamick/article-pdf/18/37/50681/6847838/am-2026-05380r.pdf by guest on 21 October 2026

sample to air during transfer to the XPS instrument likely led to partial surface oxidation, accounting for the presence of Cu(II) species detected.

Prepared Cu-based systems were further investigated using X-ray absorption spectroscopy (XAS), a technique sensitive to the oxidation state, geometry, and coordination environment around the metal centers. The Cu K-edge X-ray absorption near-edge structure (XANES) spectra are shown in Figure 2g and Figure S4, displaying significant differences among the systems, consistent with the observations from XPS and electron diffraction analyses. In the case of **Cu_2O-Cub**, the XANES spectrum exhibits an edge position at ca. 8980 eV along with a characteristic intense absorption peak at ca. 8982 eV, typical of Cu_2O materials, indicating that the sample is mainly composed of Cu(I), as the spectrum perfectly overlaps with that of the Cu_2O reference sample. On the other hand, the Cu K-edge position for **Cu_2O-PSph** lies close to the Cu(I) reference but is slightly shifted to higher energies, suggesting the presence of species with a higher oxidation state. This is also evident from the lower intensity of the characteristic Cu_2O absorption at ca. 8982 eV with respect to the Cu(I) reference. Edge fitting of the Cu K-edge XANES features for Cu_2O-PSph was performed to roughly estimate the species ratio, combining the spectra of Cu_2O and CuO in an 8.3:1.7 ratio (Figure 2h). Notably, fittings of the XANES region using mixtures containing metallic copper and oxides were unsuccessful, strongly supporting the presence of the proposed binary mixture. The analysis of the nanoparticles prepared by the organometallic approach (Figure 2i), **Cu-Org**, indicated the presence of more reduced species, with an edge position significantly shifted toward Cu(0), evidencing mixtures of copper in its metallic and oxide forms. For this system, the Cu K-edge XANES spectrum was reconstructed by combining Cu and Cu_2O spectra in a 6.2:3.7 ratio, suggesting the coexistence of both species in the bulk material. The detection of Cu(I) probably originates from surface oxidation of the nanoparticulated material upon air exposure during sample preparation for the measurements. The extended X-ray absorption fine structure (EXAFS) analysis further corroborates the trends observed by XANES. The corresponding *R*-space spectra for the Cu K-edge, fitted using the proposed structural models, are displayed in Figure S5 (see also Figure S6 and Table S1). The spectrum of **Cu_2O-Cub** is well reproduced using a Cu_2O model, whereas that of **Cu_2O-PSph** is consistent with a mixed Cu_2O/CuO composition in an 8.3:1.7 ratio. The spectra are dominated by Cu–O scattering contributions at ca. 1.87 Å and by a second intense feature centered at ca. 3.01 Å, corresponding to the first (Cu–O) and second (Cu–Cu/O) coordination shells, respectively, characteristic of Cu_2O and Cu_2O/CuO mixed phases (Table S1). In the case of **Cu-Org**, a qualitative comparative analysis of the *R*-space spectra indicates the presence of features characteristic of a Cu(0)/Cu_2O mixture, consistent with Cu–O and Cu–Cu scattering contributions in Cu_2O and metallic Cu references (see Figure S6). Unfortunately, the limited data resolution and the lack of reliable EXAFS data above $k = 9$ Å^{-1}, hinder reliable fitting of the *R*-space spectrum.

The obtained Cu-based materials represent an excellent platform to evaluate the effect of polyaromatic film (PAF) functionalization on the CO_2RR activity of Cu materials of distinct morphology and composition. Therefore, after drop-casting **Cu_2O-Cub** and **Cu_2O-PSph** on CP (**Cu-Org** is grown on this support), PAFs were prepared over the three materials by electrochemical polymerization of the diphenyliodonium ion at –0.90 V vs RHE for 10 min (Figure S7a). The chronoamperometries corresponding to the PAF formation showed a clear decrease in current density with time for all Cu-based materials (Figure S8), which suggests a change in the catalyst–electrolyte interface. The decrease in current density is expected from the generation of a hydrophobic film that limits the diffusion of water molecules and limits the number of accessible catalytic active sites.[39,58] The materials obtained after PAF electropolymerization are denoted as **Cu_2O-Cub/PAF**, **Cu_2O-PSph/PAF**, and **Cu-Org/PAF**. SEM images show that the morphology of the materials remains largely unchanged after PAF formation (Figure 1e–g), indicating that the process does not significantly alter the initial catalyst structure. However, in the case of **Cu-Org/PAF**, the presence of the polymer layer becomes evident. HRSEM images at high magnification display a loss of resolution, which is attributed to the presence of a nonconductive organic layer on the particle surface. X-ray absorption spectroscopy further revealed that all three systems underwent reduction upon PAF functionalization, as evidenced by the pronounced shift of the Cu K-edge toward lower energies. Fitting of the XANES spectra confirmed the formation of Cu(0)/Cu_2O mixtures in 1.4:8.6, 6.0:4.0, and 7.0:3.0 ratios for **Cu_2O-Cub**, **Cu_2O-PSph**, and **Cu-Org**, respectively (Figure S9). This behavior is attributed to the reductive environment required for PAF formation and to the resulting hydrophobic layer, which may help protect the Cu sites against ambient oxidation. However, as discussed below from the operando XAS measurements (Section 3.2), all PAF-functionalized catalysts evolve toward predominantly metallic Cu under CO_2RR conditions. Therefore, these ex situ oxidation-state differences reflect the catalyst state immediately after PAF electropolymerization rather than the steady-state catalyst during operation.

3.2. Electrocatalytic CO_2 Reduction in a Gas-Tight H-Cell

To evaluate the catalytic activity of the different materials and assess the effect of the PAFs, a first screening was done by using a gas-tight H-cell (Figure S7b). The linear sweep voltammetries (LSV) of the materials (Figure S10) showed in all cases an increase in the onset potential and a current density decrease in the full potential range after PAF electropolymerization. The effect on the onset potential can be expected from a change in product selectivity (from H_2 to C_1–C_{2+}), CO_2RR requiring more energy and being kinetically slower than HER in most cases.[11] The decrease in current density can be attributed to the limitation of mass transport at the catalyst–electrolyte interface.[9,58] Moreover, a significant reduction peak between –0.30 and –0.40 V vs RHE is observed for the **Cu_2O-PSph** and **Cu_2O-PSph/PAF** materials, indicating a fast reduction of existing Cu(II)/Cu(I) species to Cu(0). This peak is usually detected for materials composed of small CuO_x particles, and it is not observed for bigger crystalline particles.[59] It is also worth noticing that **Cu_2O-Cub** showed the lower current density of all materials, which is probably related to its higher particle size and its lower specific surface area.

From the LSV curves (Figure S10), four potentials were selected (–0.95, –1.05, –1.25, and –1.40 V vs RHE) to perform quantitative CO_2 reduction experiments (Figure 3a–c and Figures S11 and S13) and analyze the effect of PAFs on the product selectivity of the materials. A 1 h chronoamperometry (CA) was applied to the different materials. The only exception

Downloaded from pubs.acs.org/aamick/article-pdf/18/37/50681/6847/8387/am-2026-05380r.pdf by guest on 21 October 2026

https://doi.org/10.1021/acsami.6c05380
ACS Appl. Mater. Interfaces 2026, 18, 50681–50693

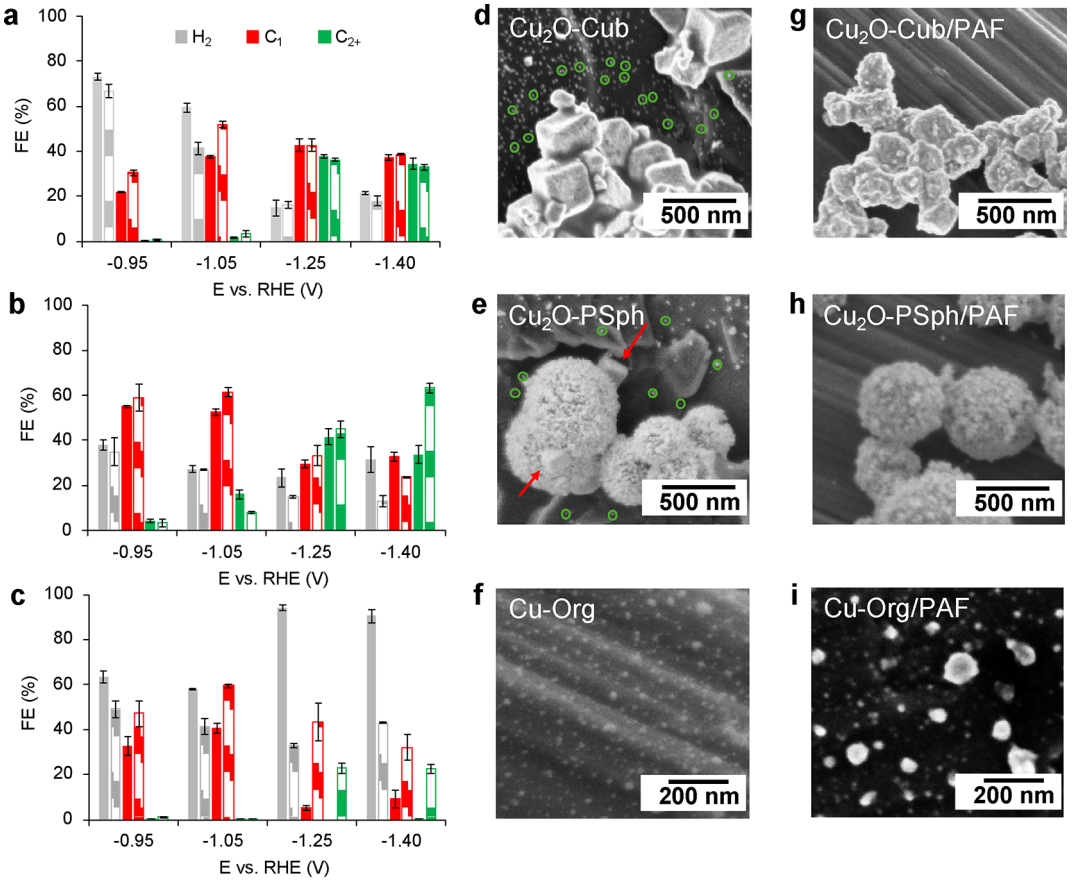

Figure 3. Faradaic efficiencies of **Cu_2O-Cub** (solid) and **Cu_2O-Cub/PAF** (dashed) (a), **Cu_2O-PSph** (solid) and **Cu_2O-PSph /PAF** (dashed) (b), and **Cu-Org** (solid) and **Cu-Org /PAF** (dashed) (c) at different applied potentials in a gas-tight H-cell using aqueous CO_2-saturated 0.10 M $KHCO_3$ as electrolyte. Corresponding HRSEM images after 1 h chronoamperometries at –0.95 V vs RHE of **Cu_2O-Cub** (d), **Cu_2O-PSph** (e), **Cu-Org** (f), **Cu_2O-Cub/PAF** (g), **Cu_2O-PSph/PAF** (h), and **Cu-Org /PAF** (i). Red arrows point to formed cubic structures, and green circles indicate that some NPs formed due to fragmentation and/or dissolution/redeposition of Cu.

was **Cu-Org** at –1.40 V vs RHE, where the high current density and copious gas evolution limited the experiment to 30 min (Figure S12). Analysis of the product selectivity of **Cu_2O-Cub** (Figure 3a and Figure S11a) shows that at –0.95 and –1.05 V, the main products are H_2, with Faradaic efficiencies (FEs) of 73–59%, together with C_1 products (CO, $HCOO^-$, and CH_4) with FEs of 22–38%. When moving to more negative potentials (–1.25 and –1.40 V), further reduced C_{2+} products (C_2H_4, C_2H_5OH, and C_3H_7OH) were also generated achieving FEs of 38–34%. Upon PAF addition, **Cu_2O-Cub/PAF** (Figure 3a and Figure S11b) showed enhanced CO_2RR performance at –0.95 and –1.05 V, achieving C_1 FE of 30 and 52%, respectively, while suppressing the HER (67 and 41% FE, respectively). At more negative potentials, the material shows similar performance to untreated **Cu_2O-Cub**. In the case of **Cu_2O-PSph** (Figure 3b and Figure S11c), the FEs for CO_2RR were higher than for HER (maximum H_2 FE of 38% at –0.95 V) in the full potential range of study. At –0.95 and –1.05 V, C_1 products dominated (53–55% FE), while at –1.25 and –1.40 V, C_{2+} products become more relevant (35–42% FE). When the PAF treatment is applied, it can be observed that **Cu_2O-PSph/PAF** (Figure 3b and Figure S11d) does not show significant changes on product selectivity at –0.95 and –1.05 V. However, at –1.25 V, an increase on C_1 and C_{2+} products is observed at the expense of HER suppression, and at –1.40 V the selectivity is radically shifted toward C_{2+} products, achieving up to 63% FE while HER is significantly suppressed (13% FE). Finally, **Cu-Org** (Figure 3c and Figure S11e) showed certain selectivity for C_1 products (33–40% FE) at –0.95 and –1.05 V and a high intrinsic selectivity toward H_2 at –1.25 and –1.40 V, reaching FEs of 90–94%. The tendency of smaller Cu nanoparticles to produce more H_2 during CO_2 electroreduction is well known and has been related to a higher proportion of undercoordinated surface sites. The presence of such sites strengthens H adsorption and favors the hydrogen evolution reaction over CO_2RR pathways, leading to increased H_2 and CO selectivity and suppressed hydrocarbon formation compared to larger particles or bulk Cu surfaces.[60] However, when the PAF film was generated on this material, **Cu-Org/PAF** (Figure 3c and Figure S11f) showed enhanced selectivity toward C_1 products at –0.95 and –1.05 V (47–59%) while HER was abated (49-41%). At –1.25 and –1.40 V, **Cu-Org/PAF** was capable of generating C_1 (32–43% FE) and C_{2+} (23% FE) products, which is much better than untreated **Cu-Org** (5–9% FE C_1 and 0% FE C_{2+}).

The morphology-dependent impact of PAF addition on Cu-based materials can, in certain cases, be rationalized by considering differences in surface structure and facet exposure. In this context, a previous study by Buonsanti and coworkers on the surface functionalization of Cu nanocrystals with organic

https://doi.org/10.1021/acsami.6c05380
ACS Appl. Mater. Interfaces 2026, 18, 50681–50693

Downloaded from pubs.acs.org/aamick/article-pdf/18/37/50681/6847838/am-2026-05380r.pdf by guest on 21 October 2026

ligands demonstrated that identical ligands can induce distinct catalytic responses depending on particle shape, highlighting the interplay between surface chemistry and crystallographic orientation.[61] In our case, the hydrophobic PAF generated on the surface of the particles is expected to hinder water diffusion and enhance CO_2 mass transport at the catalyst–electrolyte interface. To assess whether differences in catalytic behavior could arise from variations in PAF formation, additional ECSA, EIS, and water contact angle measurements were performed (Tables S3 and S4 and Figures S14–18). After PAF functionalization, all three Cu-based systems exhibit similar ECSA values (≈0.7–1 cm^2) and comparable hydrophobicity (≈120–129°), suggesting a broadly similar degree of surface modification across catalysts. Therefore, the distinct catalytic responses are unlikely to arise from major differences in PAF coverage or hydrophobicity. Instead, the effect of the PAF layer appears to depend strongly on the intrinsic morphology and dynamic restructuring behavior of the underlying Cu catalysts. This common interfacial modification explains why, at −0.95 and −1.05 V, all PAF-functionalized catalysts show increased FE toward C_1 products (Figure 3a–c). However, at more negative potentials, the trends become different for the three materials studied. **Cu_2O-Cub** and **Cu_2O-Cub/PAF** showed very similar performance, indicating that the relatively flat cubic structures do not particularly benefit from the presence of the PAF layer (Figure 3a). On the contrary, **Cu_2O-PSph/PAF** showed a great FE enhancement of up to 21% toward C_{2+} products compared to **Cu_2O-PSph** (Figure 3b). In this case, the highly porous catalyst structure formed by ∼2.4 nm Cu_2O nanoparticles may favor local confinement of CO_2RR intermediates, particularly CO, within the porous network and underneath the hydrophobic PAF layer, increasing the probability of C–C coupling and C_{2+} formation, while simultaneously suppressing methane formation (Figure S11c,d). This interfacial microenvironment engineering concept is consistent with recent studies highlighting the importance of catalyst architecture and confinement effects in steering C_{2+} selectivity in Cu-based CO_2RR systems.[62] Finally, in the case of **Cu-Org/PAF**, HER is clearly suppressed to a considerable extent compared to **Cu-Org** (Figure 3c), which allowed to reach a maximum FE of 23% toward C_{2+}. For comparison, Table S2 summarizes the impact of PAF functionalization on CO_2RR performance reported in previous studies together with the results obtained in this work, placing the observed morphology-dependent effects in the context of the current literature. It is worth noting that the available literature is predominantly restricted to PAF-modified Cu foil systems, while Cu nanoparticle–PAF configurations remain largely unexplored to date.

After assessing the effect of PAFs in product selectivity, the effect of the films on the morphological evolution of Cu-based materials was studied. In this case, *ex-situ* observation of the electrodes by SEM was done before and after the 1 h (30 min in the case of **Cu-Org**) chronoamperometries at the four studied potentials (Figure 3d–i and Figures S19–S21). As can be seen in Figure 3d, **Cu_2O-Cub** showed presence of small NPs around the original cubes, which is consistent with fragmentation and/or dissolution-redeposition processes occurring during catalysis (Figure S22). Similar restructuring phenomena have previously been reported for Cu and Cu_2O cubes, among other morphologies, by combined *ex-situ* and *in situ* studies.[42−45] In the case of **Cu_2O-Cub/PAF** (Figure 3g) the cubes exhibited changes in faced morphology together with the appearance of chunk-like features resembling agglomerates, although no particles were observed outside the original cubes. While *ex-situ* SEM does not allow direct identification of the underlying mechanism, these observations may indicate that the polymer layer influences the redistribution of soluble Cu-based species near the catalyst surface, limiting their migration to the CP fibers. For **Cu_2O-PSph** (Figure 3e), in addition to fragmentation and possible dissolution–redeposition phenomena, cubic structures were observed at the surface of the porous spheres. Similar features have been reported during CO_2RR when small Cu NPs agglomerate into transient structures that can subsequently oxidize upon air exposure after catalysis (Figure S23).[63,64] Since the present analysis was conducted *ex-situ*, the observed cubic structures may be related to analogous transient species formed under reaction conditions and modified upon exposure to atmospheric oxygen. Given that our analysis is conducted *ex-situ*, the formation of these cubic shapes is to be expected if transient structures are generated and subsequently exposed to atmospheric oxygen. Contrary to **Cu_2O-PSph** (Figure 3e), **Cu_2O-PSph/PAF** (Figure 3h) did not show particles on the CP fibers, suggesting again that the PAF layer may affect the redistribution of the dissolved Cu species during catalysis. Moreover, cubic structures were not observed in this case, which could indicate differences in nanoparticle agglomeration and/or post-catalytic oxidation processes relative to the uncoated catalyst. Finally, **Cu-Org** (Figure 3f) showed random particle aggregation and formation of isolated cubic structures (Figure S19c), similar to those observed for **Cu_2O-PSph** (Figure 3e). In contrast, **Cu-Org/PAF** (Figure 3i) displayed a different aggregation pattern, with more uniformly distributed Cu agglomerates across the CP fibers (Figure S24). To further quantify the extent of catalyst restructuring, particle size distributions (Table S5) were extracted from SEM images before and after CO_2RR (Figures S19–S21). For Cu_2O-Cub, the average particle size decreased from 225 ± 85 to 167 ± 75 nm after electrolysis, whereas Cu_2O-Cub/PAF largely preserved its initial dimensions (223 ± 37 nm). Likewise, Cu_2O-PSph decreased from 0.73 ± 0.17 to 0.49 ± 0.13 μm after catalysis, while the PAF-coated analogue exhibited a significantly smaller change (0.61 ± 0.15 μm). Moreover, the pristine catalysts showed a substantially higher density of small nanoparticles (<40 nm) on the surrounding carbon fibers than the corresponding PAF-coated samples, consistent with a greater extent of catalyst fragmentation and/or dissolution–redeposition. Although the polymer layer prevented an equivalent quantitative analysis for Cu-Org/PAF due to the reduced SEM resolution, the overall observations support the conclusion that the PAF coating mitigates catalyst restructuring during CO_2RR. Although the exact mechanism cannot be established from *ex-situ* SEM alone, the observed trends are consistent with previous reports describing coating-induced modifications in Cu dissolution-redeposition behavior during catalysis, including studies on hydrophobic SiO_2-coated Cu NPs reported by Jiang and coworkers.[30]

Finally, operando XAS was employed to investigate the evolution of the Cu oxidation state and local coordination environment of **Cu_2O-Cub**, **Cu_2O-PSph**, and **Cu-Org**, as well as their PAF-functionalized counterparts, under catalytic conditions by applying a constant potential while simultaneously monitoring the evolution of the Cu K-edge features (Figure 4 and Figure S25). The XANES spectra recorded at open circuit potential (OCP) display edge positions consistent with the

Downloaded from pubs.acs.org/aamick/article-pdf/18/37/50681/6847838/am-2026-05380r.pdf by guest on 21 October 2026

https://doi.org/10.1021/acsami.6c05380
ACS Appl. Mater. Interfaces 2026, 18, 50681−50693

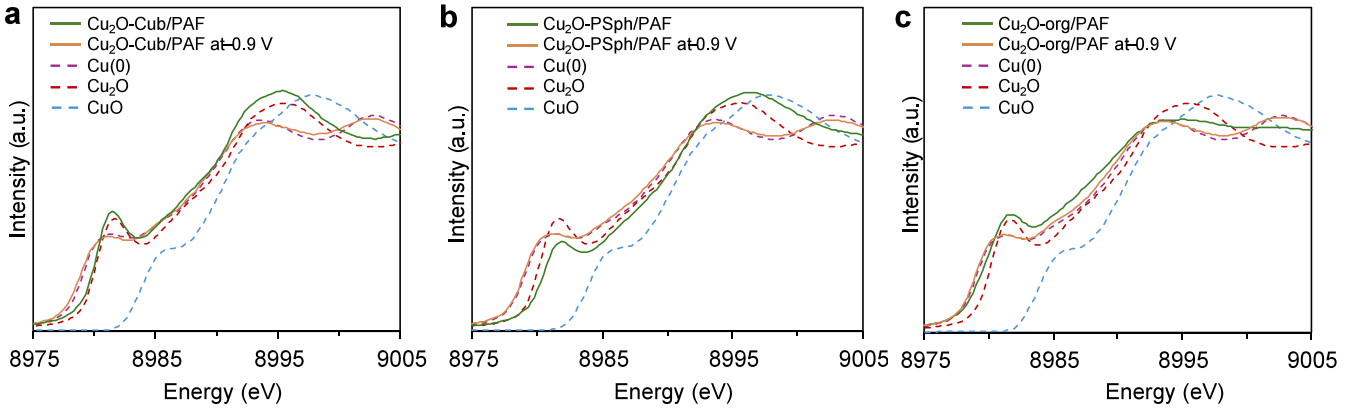

Figure 4. Normalized Cu K-edge XANES spectra of **Cu_2O-Cub/PAF** (a), **Cu_2O-PSph/PAF** (b), and **Cu-Org/PAF** (c), before and during CO_2 reduction catalysis, applying a CPE at-0.9 V vs RHE in 0.1 M $KHCO_3$ buffer at pH 7 saturated with CO_2, along with Cu(0), CuO, and Cu_2O references.

oxidation states determined in the *ex-situ* Cu K-edge analyses. Upon applying a cathodic potential within the CO_2 reduction (CO_2R) region (–0.9 V vs RHE), the Cu K-edge shifts markedly toward lower energies, evidencing the formation of species with lower oxidation states. Correlation with Cu(0) reference spectra confirms the formation of fully reduced metallic Cu species under catalytic conditions. Comparable trends were observed for all PAF-functionalized catalysts, indicating that they converge to metallic Cu under catalytic conditions. This observation suggests that the distinct CO_2RR selectivity observed for the different morphologies cannot be explained by differences in the steady-state oxidation state of Cu but rather arise from morphology-dependent interfacial effects induced by the PAF coating. It should be noted that the temporal resolution of the present operando XAS measurements does not allow the detection of short-lived Cu^+ species that may participate as reaction intermediates. Consequently, the possible involvement of transient Cu^+ sites in the abovementioned Cu dissolutionredeposition processes is inferred from the catalytic trends and previous mechanistic studies rather than from direct quantification of Cu^+ during operation.

3.3. Scale-up to a Flow Cell

To evaluate the suitability of the PAF coating strategy at higher (more practical) current densities, the transfer of this strategy to a flow cell CO_2RR setup (Figures S7c and S26) was assayed. Because the H-cell and flow cell differ substantially in electrolyte composition, CO_2 transport, local pH, and operating mode (potentiostatic vs galvanostatic), direct quantitative comparison of absolute Faradaic efficiencies is not appropriate. Instead, the flow-cell experiments were designed to evaluate whether the beneficial effect of the PAF coating is maintained under technologically relevant high-current-density conditions. From the H-cell experiments above, **Cu_2O-PSph** was selected for the scale-up test according to its superior selectivity to carbon-based products and to the clear beneficial effect of the PAF coverage to increase the FE to C_{2+} compounds.[17] The functionalization of the particles with PAFs was carried in a similar way to gas-tight cell experiments. **Cu_2O-PSph** was drop casted on the GDL, which was then submitted to the electropolymerization process at –0.90 V vs RHE for 10 min in a one-compartment cell (Figure S7a). In this case, the formation of an organic layer wrapping the particles was clearly observed by SEM (Figure 5a,b). Also here, contact angle measurements comparing untreated and PAF-functionalized electrodes demonstrated a clear increase in hydrophobicity for the functionalized surfaces, arising from the intrinsically hydrophobic polymeric layer.

In this case, CO_2RR activity was evaluated at four different current densities (j) ranging from –32 to –127 $mA{\cdot}cm^{-2}$ (Figure 5c and Figure S27), which corresponded to a potential range between –0.98 and –1.28 V vs RHE (Figure S27). Similar to the trend in H-cell configuration (Figure 3b), a clear suppression of HER was observed at all the applied current densities upon PAF functionalization (Figure 5c). **Cu_2O-PSph** showed its best performance at –64 $mA{\cdot}cm^{-2}$ (Figure 3c), where H_2 and C_{2+} FEs equaled at 32% and C_1 FE was 19%. In the case of **Cu_2O-PSph/PAF**, the best performance was found at –95 $mA{\cdot}cm^{-2}$ (Figure 5c), reaching C_{2+} FE of 52% and H_2 FE as low as 23%. At –127 $mA{\cdot}cm^{-2}$, the selectivity toward C_{2+} was still good, but the overall FE fell further from 100%, most probably because of energy losses in the form of heat. The higher apparent C_{2+} selectivity observed in the flow cell is also expected to benefit from improved CO_2 availability and altered local pH compared to the H-cell, effects that are widely recognized for gas-diffusion electrodes. Therefore, the higher apparent C_{2+} selectivity observed in the flow cell should be considered as the combined result of improved CO_2 mass transport, changes in the local reaction environment, and the intrinsic catalytic contribution of the PAF layer, rather than being attributed exclusively to PAF stabilization.

The stability of both **Cu_2O-PSph** and **Cu_2O-PSph/PAF** was evaluated at the highest current density (–127 $mA{\cdot}cm^{-2}$). The continuous monitoring of CO_2RR products over 80 min (Figure S28) revealed clear differences between the two electrodes. While the PAF-functionalized system maintained stable FEs throughout the experiment (Figure S28a), the uncoated **Cu_2O-PSph** electrode exhibited a rapid evolution of product distribution under identical conditions (Figure S28c). Specifically, the selectivity shifted from C_{2+} products toward C_1 products as electrolysis progressed, with increasing C_1 FEs occurring at the expense of multicarbon products. This trend suggests a progressive deterioration of the surface environment required for efficient C–C coupling. The stability of the PAF-modified catalyst is further supported by its preserved

Downloaded from pubs.acs.org/aamick/article-pdf/18/37/50681/6847838/am-2026-05380r.pdf by guest on 21 October 2026

https://doi.org/10.1021/acsami.6c05380
ACS Appl. Mater. Interfaces 2026, 18, 50681–50693

Figure 5. HRSEM images of the as-prepared electrodes of **Cu_2O-PSph** (a) and **Cu_2O-PSph/PAF** (b) with the corresponding CA measurements. Faradaic efficiencies of **Cu_2O-PSph** (solid) and **Cu_2O-PSph /PAF** (dashed) (c) at different applied current densities in a flow cell using aqueous CO_2-saturated 0.50 M $KHCO_3$ as electrolyte in the cathodic site.

hydrophobic character during operation (Figure S28b), which is attributed to the robust and persistent nature of the PAF layer on the Cu-based particles. Overall, these results highlight the beneficial role of PAF functionalization in sustaining stable C_{2+} production over time, consistent with the reduced extent of catalyst restructuring observed by *ex-situ* SEM for the coated systems.

4. CONCLUSIONS

This study highlights the dual role of PAF coatings in advancing CO_2RR on Cu-based catalysts. First, PAF functionalization modulates the competition between HER and CO_2RR in a catalyst- and potential-dependent manner, leading in several cases to enhanced C-based product formation, with the enhancement strongly dependent on the initial particle morphology and oxidation state. The most pronounced effect was observed for **Cu_2O-PSph/PAF**, achieving a C_{2+} Faradaic efficiency of 63% at −1.40 V vs RHE. Second, the PAF layer influences the morphological evolution of the catalysts: SEM analysis suggests reduced particle redistribution and fragmentation, together with modified aggregate formation under reaction conditions.

Importantly, this stabilization effect is also reflected in operando performance: In flow-cell experiments at high current density, PAF-coated electrodes maintain a stable product distribution over time, whereas uncoated **Cu_2O-PSph** exhibits a faster evolution of faradaic efficiencies, consistent with more pronounced catalyst restructuring in the absence of the polymer layer. These differences indicate that the PAF coating mitigates dynamic morphological changes under CO_2RR conditions while preserving its interfacial functionality, as evidenced by stable activity over 80 min with the polymer layer remaining intact.

Together, these results demonstrate that PAF functionalization can simultaneously influence selectivity, catalyst morphology, and stability under high-current-density operating conditions, with the magnitude of these effects governed by the nature of the initial Cu catalyst.

■ ASSOCIATED CONTENT

Supporting Information

The Supporting Information is available free of charge at https://pubs.acs.org/doi/10.1021/acsami.6c05380.

Morphological, spectroscopic, and electrochemical characterization together with supporting tables for size analysis, contact angle data, and comparison with reported literature (DOCX)

■ AUTHOR INFORMATION

Corresponding Authors

Antoni Llobet – *Institute of Chemical Research of Catalonia (ICIQ), Avda. Països Catalans 16, Tarragona 43007, Spain;* orcid.org/0000-0002-6176-5272; Email: allobet@iciq.cat

Xavier Sala – *Departament de Química, Unitat de Química Inorgànica, Universitat Autònoma de Barcelona, Cerdanyola del Vallès, Barcelona 08193, Spain;* orcid.org/0000-0002-7779-6313; Email: xavier.sala@uab.cat

Authors

Gerard Martí – *Departament de Química, Unitat de Química Inorgànica, Universitat Autònoma de Barcelona, Cerdanyola del Vallès, Barcelona 08193, Spain;* orcid.org/0000-0002-5888-6671

Andreina Alarcón – *Sustainable Electrochemical Processes, Departament de Ciència dels Materials i Química Física i Institut de Química Teòrica i Computacional (IQTC), Universitat de Barcelona (UB), Martí i Franquès 1, Barcelona 08028, Spain*

Matilda Kraft – *Departament de Química, Unitat de Química Inorgànica, Universitat Autònoma de Barcelona, Cerdanyola del Vallès, Barcelona 08193, Spain*

Arnau Carné-Sánchez – *Departament de Química, Unitat de Química Inorgànica, Universitat Autònoma de Barcelona, Cerdanyola del Vallès, Barcelona 08193, Spain; Catalan Institute of Nanoscience and Nanotechnology (ICN2), CSIC, and The Barcelona Institute of Science and Technology, Bellaterra, Barcelona 08193, Spain*

Marcos Gil-Sepulcre – *Departament de Química, Unitat de Química Inorgànica, Universitat Autònoma de Barcelona, Cerdanyola del Vallès, Barcelona 08193, Spain; Departament de Química Orgànica, Facultat de Química, Universitat de València, Av. Vicent Andrés Estellés 19, Burjassot 46100, Spain;* orcid.org/0000-0002-2839-8108

Olaf Rüdiger – *Max Planck Institute for Chemical Energy Conversion, Stiftstrasse 34-36, Mülheim an der Ruhr D-45470, Germany;* orcid.org/0000-0002-5148-9083

Serena DeBeer – *Max Planck Institute for Chemical Energy Conversion, Stiftstrasse 34-36, Mülheim an der Ruhr D-45470, Germany;* orcid.org/0000-0002-5196-3400

Downloaded from pubs.acs.org/aamick/article-pdf/18/37/50681/6847838/am-2026-05380r.pdf by guest on 21 October 2026

https://doi.org/10.1021/acsami.6c05380
ACS Appl. Mater. Interfaces 2026, 18, 50681−50693

Jordi García-Antón – *Departament de Química, Unitat de Química Inorgànica, Universitat Autònoma de Barcelona, Cerdanyola del Vallès, Barcelona 08193, Spain*; orcid.org/0000-0002-2401-0401

Teresa Andreu – *Sustainable Electrochemical Processes, Departament de Ciència dels Materials i Química Física i Institut de Química Teòrica i Computacional (IQTC), Universitat de Barcelona (UB), Martí i Franquès 1, Barcelona 08028, Spain*; orcid.org/0000-0002-2804-4545

Complete contact information is available at: https://pubs.acs.org/doi/10.1021/acsami.6c05380

Notes

The authors declare no competing financial interest.

■ ACKNOWLEDGMENTS

G.M. thanks the MICIU for the FPU predoctoral grant (FPU19/ 04322). X.S., J.G.-A., and T.A. thank MINECO/FEDER (PID2019-104171RB-I00) and MICIU (PID2022-138491OB-C33 and PID2023-146787OB-I00) for the financial support. AGAUR is gratefully acknowledged for the financial support (CLIMA2023-00011 and CLIMA2023-00036). M.G.-S. acknowledges support from Agencia Estatal de Investigación (RYC2024-050678-I). O.R. and S.DB. acknowledge funding by the Max Planck Society. A.C.-S. is indebted to the Ramón y Cajal Program (RYC2020-029749-I Fellowship). XAS experiments were performed at the CLAESS beamline at the ALBA Synchrotron under the proposal no. 2024098625 with the collaboration of ALBA staff. We specially acknowledge Vlad Diaconescu for his assistance during XAS experiments. A.L. acknowledges MICINN through project PID2025-168560OB-I00, Generalitat de Catalunya for the CERCA program and project 2021 SGR 01583, and Severo Ochoa (CEX2019-000925-S).

■ REFERENCES

(1) Cannon, A. J. Twelve Months at 1.5 °C Signals Earlier than Expected Breach of Paris Agreement Threshold. *Nat. Clim. Chang.* **2025**, *15* (3), 266–269.

(2) Maslin, M.; Ramnath, R. D.; Welsh, G. I.; Sisodiya, S. M. Understanding the Health Impacts of the Climate Crisis. *Future Healthc. J.* **2025**, *12* (1), No. 100240.

(3) Wu, H.; Su, X.; Huang, S.; Singh, V. P.; Zhou, S.; Tan, X.; Hu, X. Decreasing Dynamic Predictability of Global Agricultural Drought with Warming Climate. *Nat. Clim. Change* **2025**, *15*, 411–419.

(4) Nunes, L. J. R. The Rising Threat of Atmospheric CO_2: A Review on the Causes, Impacts, and Mitigation Strategies. *Environments* **2023**, *10* (4), No. 66.

(5) Geweda, A. E.; Zayed, M. E.; Khan, M. Y.; Alquaity, A. B. S. Mitigating CO_2 Emissions: A Review on Emerging Technologies/Strategies for CO_2 Capture. *J. Energy Inst.* **2025**, *118*, No. 101911.

(6) Kim, G. H.; Yang, J. W. Research Trends in CO_2 Utilization: Catalytic Strategies for Sustainable Energy and Environmental Protection. *J. CO2 Util.* **2025**, *101*, No. 103216.

(7) Leonzio, G.; Hankin, A.; Shah, N. CO_2 Electrochemical Reduction: A State-of-the-Art Review with Economic and Environmental Analyses. *Chem. Eng. Res. Des.* **2024**, *208*, 934–955.

(8) Varhade, S.; Guruji, A.; Singh, C.; Cicero, G.; García-Melchor, M.; Helsen, J.; Pant, D. Electrochemical CO_2 Reduction: Commercial Innovations and Prospects. *ChemElectroChem* **2025**, *12* (2), No. e202400512.

(9) Martí, G.; Mallón, L.; Romero, N.; Francàs, L.; Bofill, R.; Philippot, K.; García-Antón, J.; Sala, X. Surface-Functionalized Nanoparticles as Catalysts for Artificial Photosynthesis. *Adv. Energy Mater.* **2023**, *13* (21), No. 2300282.

(10) Zhang, L.; Li, Z.; Gao, Y.; Li, Q.; Deng, Z.; Miao, B.; He, H.; Poh, C. K.; Zhang, L.; Chan, S. H. Recent Advances in Supported Metal Catalysts for CO_2 Methanation: Mechanisms, Materials Design, and the Promise of Perovskite-Based Supports. *Energy Convers. Manage.:X* **2025**, *27*, No. 101066.

(11) Khalil, M.; Kadja, G. T. M.; Nugroho, F. A. A.; Sutanto, L. G.; Jiwanti, P. K.; Abdi, F. F.; Hussin, F.; Aroua, M. K. Suppressing the Competing Hydrogen Evolution Reaction in CO_2 Electroreduction: A Review. *Renewable Sustainable Energy Rev.* **2024**, *206*, No. 114869.

(12) Zhao, M.; Tang, H.; Yang, Q.; Gu, Y.; Zhu, H.; Yan, S.; Zou, Z. Inhibiting Hydrogen Evolution Using a Chloride Adlayer for Efficient Electrochemical CO_2 Reduction on Zn Electrodes. *ACS Appl. Mater. Interfaces* **2020**, *12* (4), 4565–4571.

(13) Qin, X.; Sechi, R.; Hansen, H. A. Recent Progress in Mechanistic Insights into Cation Effects on Electrochemical CO_2 Reduction Reactions. *Curr. Opin. Electrochem.* **2025**, *49*, No. 101614.

(14) Gu, Z.; Zhu, J.; Xue, Z.; Liu, X.; Shi, L.; Huang, M.; Zhu, J.; Jiang, H. Challenges and Strategies for CO_2 Electroreduction to C2+ Products under Acidic Conditions. *Green Carbon* **2025**, No. S2950155525000527.

(15) Shi, X.-D.; Guo, R.; Cui, H.; Liu, C.; Pan, W. Electrocatalytic Reduction of CO_2 to Produce the C2+ Products: From Selectivity to Rational Catalyst Design. *Nanoscale* **2025**, *17* (8), 4338–4364.

(16) Chang, F.; Xiao, M.; Miao, R.; Liu, Y.; Ren, M.; Jia, Z.; Han, D.; Yuan, Y.; Bai, Z.; Yang, L. Copper-Based Catalysts for Electrochemical Carbon Dioxide Reduction to Multicarbon Products. *Electrochem. Energy Rev.* **2022**, *5* (3), No. 4.

(17) Sun, J. W.; Fu, H. Q.; Liu, P. F.; Chen, A.; Liu, P.; Yang, H. G.; Zhao, H. Advances and Challenges in Scalable Carbon Dioxide Electrolysis. *EES Catal.* **2023**, *1* (6), 934–949.

(18) Li, S.; Zhang, Z.; Yang, D.; Li, S.; Yang, L.; Yan, W.; Xu, H. Tandem Modulation Strategy for Copper-Based Catalysts: Towards Efficient C-C Coupling in the Electrochemical Reduction of Carbon Dioxide. *J. Environ. Sci.* **2025**, *156*, 267–287.

(19) Jiang, G.; Han, D.; Han, Z.; Gao, J.; Wang, X.; Weng, Z.; Yang, Q.-H. Rational Manipulation of Intermediates on Copper for CO_2 Electroreduction Toward Multicarbon Products. *Trans. Tianjin Univ.* **2022**, *28* (4), 265–291.

(20) Xiong, R.-Z.; Xu, H.-M.; Zhu, H.-R.; Zhang, Z.-J.; Li, G.-R. Recent Progress in Cu-Based Electrocatalysts for CO2 Reduction. *Chem. Eng. J.* **2025**, *505*, No. 159210.

(21) De Gregorio, G. L.; Burdyny, T.; Loiudice, A.; Iyengar, P.; Smith, W. A.; Buonsanti, R. Facet-Dependent Selectivity of Cu Catalysts in Electrochemical CO_2 Reduction at Commercially Viable Current Densities. *ACS Catal.* **2020**, *10* (9), 4854–4862.

(22) Jun, M.; Kundu, J.; Kim, D. H.; Kim, M.; Kim, D.; Lee, K.; Choi, S. Strategies to Modulate the Copper Oxidation State Toward Selective C2+ Production in the Electrochemical CO2 Reduction Reaction. *Adv. Mater.* **2024**, *36* (21), No. 2313028.

(23) Zhang, Y.; Özden, A.; Gao, L.; Hofmann, J. P.; Hensen, E. J. M. The Role of Copper-Oxide Species in Copper-Catalyzed Electrochemical CO_2 Reduction. *Chem Electro Chem* **2025**, *12* (18), No. e202500032.

(24) Bai, X.; Tang, T.; Bai, X.; Zhang, S.; Duan, Y.; Bai, F.; Guan, J. Tuning the Electronic Structure of Copper in Bimetallic Oxyhydroxide Nanosheets for Selective Electroreduction of Carbon Dioxide. *Sci. China: Chem.* **2026**, *69* (2), 953–960.

(25) Bai, X.; Tang, T.; Sun, J.; Bai, F.; Hu, J.; Guan, J. Engineering D-Band Structure of Zn-Doped CuO H for Boosting CO_2 Electroreduction Performance. *Chin. J. Catal.* **2026**, *80*, 248–257.

(26) Xu, X.; Guan, J. Synergistic Effects in the Electrochemical Carbon Dioxide Reduction Reaction for Multi-Carbon Product Formation. *Adv. Funct. Mater.* **2025**, *35* (36), No. 2505823.

(27) Zhuang, T.-T.; Pang, Y.; Liang, Z.-Q.; Wang, Z.; Li, Y.; Tan, C.-S.; Li, J.; Dinh, C. T.; De Luna, P.; Hsieh, P.-L.; Burdyny, T.; Li, H.-H.; Liu, M.; Wang, Y.; Li, F.; Proppe, A.; Johnston, A.; Nam, D.-H.; Wu, Z.-Y.; Zheng, Y.-R.; Ip, A. H.; Tan, H.; Chen, L.-J.; Yu,

Downloaded from pubs.acs.org/aamick/article-pdf/18/37/50681/6847/8387/am-2026-05380r.pdf by guest on 21 October 2026

S.-H.; Kelley, S. O.; Sinton, D.; Sargent, E. H. Copper Nanocavities Confine Intermediates for Efficient Electrosynthesis of C3 Alcohol Fuels from Carbon Monoxide. *Nat. Catal.* **2018**, *1* (12), 946–951.
(28) Zhong, Y.; Kong, X.; Song, Z.; Liu, Y.; Peng, L.; Zhang, L.; Luo, X.; Zeng, J.; Geng, Z. Adjusting Local CO Confinement in Porous-Shell Ag@Cu Catalysts for Enhancing C–C Coupling toward CO_2 Eletroreduction. *Nano Lett.* **2022**, *22* (6), 2554–2560.
(29) Shi, H.; Luo, L.; Li, C.; Li, Y.; Zhang, T.; Liu, Z.; Cui, J.; Gu, L.; Zhang, L.; Hu, Y.; Li, H.; Li, C. Stabilizing Cu+ Species in Cu_2O/CuO Catalyst via Carbon Intermediate Confinement for Selective CO_2RR. *Adv. Funct. Mater.* **2024**, *34* (11), No. 2310913.
(30) Wang, M.; Wang, Z.; Huang, Z.; Fang, M.; Zhu, Y.; Jiang, L. Hydrophobic SiO2 Armor: Stabilizing Cuδ+ to Enhance CO_2 Electroreduction toward C2+ Products in Strong Acidic Environments. *ACS Nano* **2024**, *18* (23), 15303–15311.
(31) Ren, S.; Cao, X.; Fan, Q.; Yang, Z.; Wang, F.; Wang, X.; Bai, L.; Yang, J. Selective CO_2 Electroreduction to Multi-Carbon Products on Organic-Functionalized CuO Nanoparticles by Local Micro-Environment Modulation. *Nano Micro Lett.* **2024**, *16* (1), No. 262.
(32) Peng, Y.; Zhan, C.; Jeon, H. S.; Frandsen, W.; Cuenya, B. R.; Kley, C. S. Organic Thin Films Enable Retaining the Oxidation State of Copper Catalysts during CO2 Electroreduction. *ACS Appl. Mater. Interfaces* **2024**, *16* (5), 6562–6568.
(33) Tan, D.; Feng, Y.; Zhang, J. Surface Modification Strategies for Copper-Based Catalysts in Selective CO_2 Electroreduction to Multicarbon Products. *ACS Energy Lett.* **2025**, *10* (9), 4221–4241.
(34) Ding, P.; An, H.; Zellner, P.; Guan, T.; Gao, J.; Müller-Buschbaum, P.; Weckhuysen, B. M.; Van Der Stam, W.; Sharp, I. D. Elucidating the Roles of Nafion/Solvent Formulations in Copper-Catalyzed CO_2 Electrolysis. *ACS Catal.* **2023**, *13* (8), 5336–5347.
(35) Chang, M.; Ren, W.; Ni, W.; Lee, S.; Hu, X. Ionomers Modify the Selectivity of Cu-Catalyzed Electrochemical CO2 Reduction. *ChemSusChem* **2023**, *16* (5), No. e202201687.
(36) Liu, G.; McLaughlin, D.; Thiele, S.; Van Pham, C. Correlating Catalyst Ink Design and Catalyst Layer Fabrication with Electrochemical CO_2 Reduction Performance. *Chem. Eng. J.* **2023**, *460*, No. 141757.
(37) Nie, W.; Heim, G. P.; Watkins, N. B.; Agapie, T.; Peters, J. C. Organic Additive-derived Films on Cu Electrodes Promote Electrochemical CO_2 Reduction to C2+ Products Under Strongly Acidic Conditions. *Angew. Chem., Int. Ed.* **2023**, *62* (12), No. e202216102.
(38) Venkatkarthick, R.; Lima, F. H. B. Polythiophene-Decorated Copper via Polypyrrole Intermediary Passivation Layer for Enhanced Electrocatalytic Reduction of Carbon Dioxide. *J. Electroanal. Chem.* **2024**, *961*, No. 118241.
(39) Watkins, N. B.; Wu, Y.; Nie, W.; Peters, J. C.; Agapie, T. *In Situ* Deposited Polyaromatic Layer Generates Robust Copper Catalyst for Selective Electrochemical CO_2 Reduction at Variable pH. *ACS Energy Lett.* **2023**, *8* (1), 189–195.
(40) Wu, Z.-Z.; Yang, P.-P.; Gao, M.-R. Dynamic Evolution of Copper-Based Catalysts during CO_2 Electroreduction. *Nano Mater. Sci.* **2024**, *8*, 687–702.
(41) Zhong, Y.; Sun, Z.; Xia, B. Y.; Su, Y. Structural Reconstruction of Copper-Based Catalysts in CO_2 Electroreduction Reaction: A Comprehensive Review. *Chem. Eur. J.* **2025**, *31* (27), No. e202500770.
(42) Jung, H.; Lee, S. Y.; Lee, C. W.; Cho, M. K.; Won, D. H.; Kim, C.; Oh, H.-S.; Min, B. K.; Hwang, Y. J. Electrochemical Fragmentation of Cu_2O Nanoparticles Enhancing Selective C–C Coupling from CO_2 Reduction Reaction. *J. Am. Chem. Soc.* **2019**, *141* (11), 4624–4633.
(43) Vavra, J.; Shen, T.; Stoian, D.; Tileli, V.; Buonsanti, R. Real-time Monitoring Reveals Dissolution/Redeposition Mechanism in Copper Nanocatalysts during the Initial Stages of the CO_2 Reduction Reaction. *Angew. Chem., Int. Ed.* **2021**, *60* (3), 1347–1354.
(44) Vavra, J.; Ramona, G. P. L.; Dattila, F.; Kormányos, A.; Priamushko, T.; Albertini, P. P.; Loiudice, A.; Cherevko, S.; Lopéz, N.; Buonsanti, R. Solution-Based Cu+ Transient Species Mediate the Reconstruction of Copper Electrocatalysts for CO_2 Reduction. *Nat. Catal.* **2024**, *7* (1), 89–97.
(45) Grosse, P.; Yoon, A.; Rettenmaier, C.; Herzog, A.; Chee, S. W.; Roldan Cuenya, B. Dynamic Transformation of Cubic Copper Catalysts during CO_2 Electroreduction and Its Impact on Catalytic Selectivity. *Nat. Commun.* **2021**, *12* (1), No. 6736.
(46) Grosse, P.; Gao, D.; Scholten, F.; Sinev, I.; Mistry, H.; Roldan Cuenya, B. Dynamic Changes in the Structure, Chemical State and Catalytic Selectivity of Cu Nanocubes during CO_2 Electroreduction: Size and Support Effects. *Angew. Chem., Int. Ed.* **2018**, *57* (21), 6192–6197.
(47) Mom, R. V.; Sandoval-Diaz, L.-E.; Gao, D.; Chuang, C.-H.; Carbonio, E. A.; Jones, T. E.; Arrigo, R.; Ivanov, D.; Hävecker, M.; Roldan Cuenya, B.; Schlögl, R.; Lunkenbein, T.; Knop-Gericke, A.; Velasco-Vélez, J.-J. Assessment of the Degradation Mechanisms of Cu Electrodes during the CO_2 Reduction Reaction. *ACS Appl. Mater. Interfaces* **2023**, *15* (25), 30052–30059.
(48) Gao, Y.; Wu, Q.; Liang, X.; Wang, Z.; Zheng, Z.; Wang, P.; Liu, Y.; Dai, Y.; Whangbo, M.; Huang, B. Cu_2O Nanoparticles with Both {100} and {111} Facets for Enhancing the Selectivity and Activity of CO_2 Electroreduction to Ethylene. *Adv. Sci.* **2020**, *7* (6), No. 1902820.
(49) Zhang, Z.; Che, H.; Wang, Y.; Gao, J.; Zhao, L.; She, X.; Sun, J.; Gunawan, P.; Zhong, Z.; Su, F. Facile Synthesis of Mesoporous Cu2O Microspheres with Improved Catalytic Property for Dimethyldichlorosilane Synthesis. *Ind. Eng. Chem. Res.* **2012**, *51* (3), 1264–1274.
(50) Barrière, C.; Piettre, K.; Latour, V.; Margeat, O.; Turrin, C.-O.; Chaudret, B.; Fau, P. Ligand Effects on the Air Stability of Copper Nanoparticles Obtained from Organometallic Synthesis. *J. Mater. Chem.* **2012**, *22* (5), 2279–2285.
(51) Rüdiger, O.; Gil Sepulcre, M.; Huang, G.; Laurich, C.; DeBeer, S. X-Ray Spectroelectrochemical Flow Cell. In *Edmond* **2026**.
(52) Ravel, B.; Newville, M. *ATHENA, ARTEMIS, HEPHAESTUS*: Data Analysis for X-Ray Absorption Spectroscopy Using *IFEFFIT*. *J. Synchrotron Rad.* **2005**, *12* (4), 537–541.
(53) Chen, B.; Kumar, G.; Wei, Y.; Ma, H.; Kao, J.; Chou, P.; Chuang, Y.; Chen, I.; Chou, J.; Lo, Y.; Huang, M. H. Experimental Revelation of Surface and Bulk Lattices in Faceted Cu_2O Crystals. *Small* **2023**, *19* (44), No. 2303491.
(54) Li, J.; Mei, Z.; Liu, L.; Liang, H.; Azarov, A.; Kuznetsov, A.; Liu, Y.; Ji, A.; Meng, Q.; Du, X. Probing Defects in Nitrogen-Doped Cu_2O. *Sci. Rep.* **2014**, *4* (1), No. 7240.
(55) Li, X.; Kong, W.; Qin, X.; Qu, F.; Lu, L. Self-Powered Cathodic Photoelectrochemical Aptasensor Based on in Situ–Synthesized CuO-Cu_2O Nanowire Array for Detecting Prostate-Specific Antigen. *Microchim. Acta* **2020**, *187* (6), No. 325.
(56) Gražulis, S.; Chateigner, D.; Downs, R. T.; Yokochi, A. F. T.; Quirós, M.; Lutterotti, L.; Manakova, E.; Butkus, J.; Moeck, P.; Le Bail, A. Crystallography Open Database – an Open-Access Collection of Crystal Structures. *J. Appl. Crystallogr.* **2009**, *42* (4), 726–729.
(57) Thommes, M.; Kaneko, K.; Neimark, A. V.; Olivier, J. P.; Rodriguez-Reinoso, F.; Rouquerol, J.; Sing, K. S. W. Physisorption of Gases, with Special Reference to the Evaluation of Surface Area and Pore Size Distribution (IUPAC Technical Report). *Pure Appl. Chem.* **2015**, *87* (9–10), 1051–1069.
(58) Zhao, T.; Zhou, Z.; Wang, X.; Liu, K.; Chen, J.; Liu, K.; Li, Y.; Yu, M.; Xu, Y.; Yan, Z.; Jiao, L.; Cheng, F. Tailoring Dual-Hydrophobic Microenvironment for Tandem CO_2/CO Feedstock to Enhance CO_2 Electroreduction on Cu-Based Catalysts. *Chem. Sci.* **2025**, *16* (31), 14207–14215.
(59) Liu, B.; Cai, C.; Yang, B.; Chen, K.; Long, Y.; Wang, Q.; Wang, S.; Chen, G.; Li, H.; Hu, J.; Fu, J.; Liu, M. Intermediate Enrichment Effect of Porous Cu Catalyst for CO_2 Electroreduction to C2 Fuels. *Electrochim. Acta* **2021**, *388*, No. 138552.
(60) Reske, R.; Mistry, H.; Behafarid, F.; Roldan Cuenya, B.; Strasser, P. Particle Size Effects in the Catalytic Electroreduction of CO_2 on Cu Nanoparticles. *J. Am. Chem. Soc.* **2014**, *136* (19), 6978–6986.
(61) Pankhurst, J. R.; Iyengar, P.; Okatenko, V.; Buonsanti, R. Copper Nanocrystal Morphology Determines the Viability of Molecular Surface Functionalization in Tuning Electrocatalytic Behavior in CO_2 Reduction. *Inorg. Chem.* **2021**, *60* (10), 6939–6945.

Downloaded from pubs.acs.org/aamick/article-pdf/18/37/50681/6847838/am-2026-05380r.pdf by guest on 21 October 2026

https://doi.org/10.1021/acsami.6c05380
ACS Appl. Mater. Interfaces 2026, 18, 50681–50693

(62) Hu, J.; Chen, X.; Liu, J.; Guan, J. Advances in the CO_2 Electroreduction to Multi-Carbon Products. *Chem. Eng. J.* **2025**, *516*, No. 164199.
(63) Yang, Y.; Louisia, S.; Yu, S.; Jin, J.; Roh, I.; Chen, C.; Fonseca Guzman, M. V.; Feijóo, J.; Chen, P.-C.; Wang, H.; Pollock, C. J.; Huang, X.; Shao, Y.-T.; Wang, C.; Muller, D. A.; Abruña, H. D.; Yang, P. Operando Studies Reveal Active Cu Nanograins for CO_2 Electroreduction. *Nature* **2023**, *614* (7947), 262–269.
(64) Yang, Y.; Shi, C.; Feijóo, J.; Jin, J.; Chen, C.; Han, Y.; Yang, P. Dynamic Evolution of Copper Nanowires during CO_2 Reduction Probed by Operando Electrochemical 4D-STEM and X-Ray Spectroscopy. *J. Am. Chem. Soc.* **2024**, *146* (33), 23398–23405.

Downloaded from pubs.acs.org/aamick/article-pdf/18/37/50681/6847838/am-2026-05380r.pdf by guest on 21 October 2026

https://doi.org/10.1021/acsami.6c05380
ACS Appl. Mater. Interfaces 2026, 18, 50681−50693